Geophysical Journal International

Geophys. J. Int. (2023) **235,** 2888–2899
Advance Access publication 2023 October 14
Applied and Marine Geophysics

https://doi.org/10.1093/gji/ggad398

Comparison of different inversion strategies for electrical impedance tomography (EIT) measurements

Haoran Wang [1], Egon Zimmermann,[2] Maximilian Weigand,[3] Harry Vereecken[1] and Johan Alexander Huisman[1]

[1] *Agrosphere (IBG 3), Institute of Bio- and Geosciences, Forschungszentrum Jülich GmbH, 52428 Jülich, Germany. E-mail: h.wang@fz-juelich.de*
[2] *Electronic systems (ZEA-2), Central Institute of Engineering Electronics and Analytics, Forschungszentrum Jülich GmbH, 52428 Jülich, Germany*
[3] *Geophysics Section, Institute of Geosciences, University of Bonn, 53115 Bonn, Germany*

Accepted 2023 October 6. Received 2023 October 6; in original form 2023 July 24

SUMMARY

Electrical impedance tomography (EIT) is a promising method to image the frequency-dependent complex electrical conductivity distribution of the subsurface in the mHz to kHz frequency range. In contrast to the well-developed electrical resistivity tomography (ERT) method, the inversion approach for EIT data is less established. Different inversion strategies have been proposed, but the implications of the differences between these methods have not been investigated yet. In this study, we aim to compare four different inversion strategies for EIT measurements. The first strategy (CVI) formulates the inverse problem in the complex number domain and is mathematically the most elegant method. The second strategy (RVI) is the established real-valued inversion method, which decouples the inversion of the real and imaginary parts and completely ignores the complex nature. The third strategy (ALT) is very similar to the RVI strategy in case of small phase angles, but it considers the complex coupling in the forward operator and alternately updates the real and imaginary parts of the model in the case of large phase angles. The fourth and final strategy (CVI+) was newly formulated in this study. It fully considers the complex nature of EIT measurements but separates the treatment of the real and imaginary part in terms of the data weighting and regularization. The different inversion strategies were tested with two synthetic models. The first model has a small phase contrast and the second model has a large phase contrast. In the case of a small phase contrast, the CVI strategy was able to resolve the distribution of electrical conductivity amplitude, but the inversion result for the phase angle was less reliable. The other three strategies presented similar results and the models were well resolved within the expected data misfit. In the case of a model with large phase contrast, only the newly formulated CVI + strategy was able to produce reliable results. It was found that the extremely large phase angle can have a significant influence on the modelled amplitude of data. The cross-sensitivity (i.e. the imaginary part of the sensitivity) that describes the influence on the real part of data due to a change in the imaginary part of model, or that on the imaginary part of data due to a change in the real part of model, provided unique information during the inversion. It was concluded that the CVI + strategy is theoretically the most comprehensive and correct approach for EIT inversion, but that in the case of small phase angles the RVI strategy has the practical advantage that no complex calculations are required, which substantially reduces the required computational effort.

Key words: Electrical properties; Inverse theory; Tomography; Hydrogeophysics.

1. INTRODUCTION

Electrical impedance tomography (EIT) has received increased attention in recent years given its promising capability to image the subsurface complex electrical conductivity distribution in a broad frequency range (i.e. mHz to kHz). Laboratory studies of induced polarization (IP) mechanisms (Revil & Florsch 2010; Bücker & Hördt 2013; Revil *et al.* 2017), development of advanced measurement systems (Zimmermann *et al.* 2008, 2010), and efforts in electromagnetic coupling removal (Dahlin & Leroux 2012; Schmutz

et al. 2014; Zhao *et al.* 2015; Wang *et al.* 2021) have prompted the application of frequency domain measurements (EIT) as well as time domain IP measurements at the field scale in different contexts. This includes contaminated site characterization (Flores Orozco *et al.* 2012a), plant root system imaging (Weigand & Kemna 2019), geochemical process monitoring (Doetsch *et al.* 2015) and the determination of permeability and lithology (Attwa & Günther 2013; Maurya *et al.* 2018).

Considerable attention has been paid to improving the accuracy of EIT measurements, including the development of advanced measurement systems (Radic 2004; Zimmermann *et al.* 2008) and the removal of electromagnetic coupling effects (Schmutz *et al.* 2014; Zhao *et al.* 2015; Flores Orozco *et al.* 2021; Wang *et al.* 2021). However, it is well known that a proper inversion strategy is equally important for obtaining reliable imaging results. Different from the inversion of electrical resistivity tomography (ERT) data where only the amplitude of the measurements is considered, the inversion of EIT data deals with complex measurements involving the amplitude and phase (or real and imaginary parts) of the measured impedances. Early work on the inversion of time-domain induced polarization (TDIP) data linearized the chargeability in the inverse problem and used a formulation in the real number domain (Oldenburg & Li 1994; Beard *et al.* 1996). In the frequency domain, complex-valued forward modelling (Weller *et al.* 1996b) enabled a complex inversion (Weller *et al.* 1996a). However, Weller *et al.* (1996a) inverted the complex data using a simultaneous iterative reconstruction technique, which was developed for linear problems. Based on the nonlinear Gauss-Newton method that is widely adopted in the inversion of DC resistivity data (Sasaki 1992; LaBrecque *et al.* 1996; Loke & Barker 1996), a direct complex inversion strategy with the data and model in complex form can be formulated. For this case, Kemna (2000) showed that the inversion was dominated by the real part of the data and model. Therefore, an additional inversion step called the final phase improvement (FPI) was proposed by Kemna (2000) to separately refine the phase model using the real part of the final complex Jacobian from the first step. Recent developments in the inversion of EIT data have tried to simplify and separate the inversion of real and imaginary parts to a larger extent. Martin & Günther (2013) adopted a two-step real-valued inversion approach where the amplitude was inverted first in the real number domain (i.e. ERT inversion), and the imaginary resistivity was then separately inverted using the final real-valued Jacobian from the first step. It should be noted that the calculated sensitivity or Jacobian is complex based on a complex model. The real part of the complex sensitivity describes the change in the real part of the measured data due to a change in the real part of the model parameters, or that in the imaginary part of the measured data due to a change in the imaginary part of the model parameters. The imaginary part of the complex sensitivity, also called the cross-sensitivity, describes the change in the real part of the measured data due to a change in the imaginary part of the complex model, or that in the imaginary part of the measured data due to a change in the real part of the complex model. The strategy proposed by Martin & Günther (2013) can be referred to as a two-step inversion. It ignores the cross-sensitivity (i.e. imaginary part of the sensitivity) and relies on the assumption of small phase angles. Although measured phase angles are mostly small for near surface applications, large phase angles were also occasionally reported. For example, Kulenkampff & Yaramanci (1993) showed that the measured phase angle for rock salt can be extremely large with phase values up to 1000 mrad. Recently, Peruzzo *et al.* (2021) presented large phase angles above 500 mrad for wheat plant root system.

Johnson & Thomle (2018) proposed a decoupled strategy for the inversion of EIT measurements, which is especially beneficial for large-scale problems because the complex forward modelling was decomposed and can be done in the real number domain. In particular, the imaginary part of the potential distribution was obtained in the real number domain after the real part of the potential was solved. In the case of phase angle below 200 mrad, their approach becomes again a two-step inversion. For large phase angles, it alternately inverts for the real and imaginary part of the complex electrical conductivity using the decoupled forward modelling and approximated sensitivity. Although this approach used a decoupled forward calculation approach to provide accurate forward modelling in a computationally efficient way, the cross-sensitivity was again ignored. The real part of the complex sensitivity was approximated based on the reciprocity theorem (Geselowitz 1971) using only the real part of the potential distribution. However, it should be noted that the real part of the sensitivity presented in Eq. (B3) of Johnson & Thomle (2018) should include the contribution of the imaginary part of the potential distribution in the case of models with large phase values. Unfortunately, the inversion strategy proposed by Johnson & Thomle (2018) was only tested with models showing small phase values. It remains to be seen how this alternate inversion strategy performs and whether the cross-sensitivity can be neglected in the case of models with large phase values.

Based on these previous studies, the inversion approaches for EIT data can be divided into three strategies. The first strategy is the direct complex inversion where the data and model are complex numbers. The second strategy is a two-step inversion approach that separately inverts the real and imaginary parts of the considered data while ignoring their complex nature. The third strategy is an alternate inversion approach that updates the real and imaginary parts of the considered model alternately in each iteration and is specially designed to deal with large phase angles. Although the drawbacks of the first strategy have been pointed out before (Kemna 2000; Günther & Martin 2016), it remains to be explained in detail how the real part of the data and model dominate the inversion. The second and the third strategy consider the separated treatment of the real and imaginary part of the complex data and model in terms of data weighting and model regularization to some extent, but they do not fully consider the complex nature of EIT data inversion. The cross-sensitivity has always been neglected so far, but this simplification needs further investigation for the case that the measurements show large phase angles. The theoretically ideal case for EIT inversion should consider simultaneously the coupling between real and imaginary parts of the complex data and model, and the separated treatment in terms of data weighting and model regularization. To the best of our knowledge, such an approach has not been presented yet. In addition, the implications of using different inversion strategies for EIT imaging have not been investigated yet.

In this context, the aim of this work is twofold. We first aim to develop an inversion strategy that can fully account for the intrinsic complex nature of EIT data inversion while considering a separated treatment in terms of data weighting and model regularization. In a second step, we then aim to compare different inversion strategies and discuss their limitations. In the following sections, we will first describe in detail the different inversion approaches considered in this study. After this, the different approaches will be compared using a synthetic modelling study with both small and large phase models.

2. MATERIALS AND METHODS

2.1 Forward modelling

The forward problem in EIT involves solving the Poisson equation for a given complex electrical conductivity distribution and measurement configuration:

$$\nabla \cdot (\boldsymbol{\sigma}^* \nabla \phi^*) = -\nabla \cdot \mathbf{J}, \tag{1}$$

where $\boldsymbol{\sigma}^*$ is the complex electrical conductivity of the medium, ϕ^* is the complex potential and J is the source current density. In this study, eq. (1) was solved in 2.5-D (Dey & Morrison 1979) where the change of electrical conductivity along the direction perpendicular to the inversion plane is assumed to be zero. A custom-made Matlab program extended from Zimmermann (2011) was used to solve the forward problem using the finite element method (FEM). Neumann (no-flow) boundary conditions were applied to all domain boundaries and the subsurface boundaries were put sufficiently far away from the survey area of interest. The 2-D unstructured grids were generated using Gmsh (Geuzaine & Remacle 2009). The modelling grid was refined around the electrodes by adding nine additional nodes between two neighbouring electrodes and the element size gradually increased with increasing distance from the electrodes.

2.2 General formulation of the inverse problem

Since the inversion approaches discussed in this study are all based on a Gauss–Newton scheme, we first illustrate this part of the inversion in general and then describe the specific parameters and decisions in each EIT inversion approach. The inversion aims to iteratively minimize the following objective function:

$$\Phi = ||\boldsymbol{W_d}(\boldsymbol{d} - f(\boldsymbol{m}))||^2 + \lambda ||\boldsymbol{W_m}\boldsymbol{m}||^2, \tag{2}$$

where $\boldsymbol{d}$ is a vector with the measured data, $\boldsymbol{m}$ is a vector with model parameters, $f(\boldsymbol{m})$ is the forward response of model $\boldsymbol{m}$, $\boldsymbol{W_d}$ is the diagonal data weighting matrix, that is $\boldsymbol{W_d} = diag(1/\boldsymbol{e})$ and $\boldsymbol{e}$ is the data weighting vector containing the expected standard deviation of the data, λ is the damping factor and $\boldsymbol{W_m}$ is the regularization matrix used to specify the desired properties of the model $\boldsymbol{m}$. To obtain $\boldsymbol{W_m}$, the number of immediate neighbour elements n for the ith element was counted. A value of 1 is assigned to the ith diagonal position in $\boldsymbol{W_m}$ and a value of '$-1/n$' is assigned to the neighbouring elements at the corresponding position in $\boldsymbol{W_m}$ (Chou *et al.* 2016). Using a linear Taylor series approximation and differentiating the total objective function with respect to $\Delta\boldsymbol{m}$ results in the following model update equation (Park & Van 1991; Li & Oldenburg 1999):

$$\begin{aligned}&\left(\boldsymbol{G}^T\boldsymbol{W}_d^T\boldsymbol{W}_d\boldsymbol{G} + \lambda\boldsymbol{W}_m^T\boldsymbol{W}_m\right)\Delta\boldsymbol{m}\\ &\quad = \boldsymbol{G}^T\boldsymbol{W}_d^T\boldsymbol{W}_d\left(\boldsymbol{d} - f(\boldsymbol{m})\right) - \lambda\boldsymbol{W}_m^T\boldsymbol{W}_m\boldsymbol{m},\end{aligned} \tag{3}$$

where $\boldsymbol{G}$ is the Jacobian matrix and T indicates the transpose of a matrix.

The inversion starts from a homogeneous model determined based on the mean value of the measurements (i.e. mean value of apparent electrical conductivity and phase). The damping factor λ that controls the strength of the regularization is a key parameter in the inversion. There are different methods to determine the appropriate regularization strength, including the discrepancy, the generalized cross-validation (GCV) and the L-curve method (Vogel 2002; Farquharson & Oldenburg 2004). When data error estimates are available as is the case in this study, the discrepancy method that tries to minimize the data misfit to the expected data error typically is the preferred choice (Vogel 2002; Günther 2004). In this study, we started the inversion with a large damping factor estimated from the row sums of the matrix product $\boldsymbol{G}^T\boldsymbol{W}_d^T\boldsymbol{W}_d\boldsymbol{G}$ and gradually reduced it to reach the target data misfit. The damping factor λ was iteratively reduced based on the data misfit using the scheme proposed by Kemna (2000). In particular, the decrease of λ was fast in the beginning of the inversion when the normalized data misfit χ^2 is high and slowed down when χ^2 is approaching the expected range ($0.95 < \chi^2 < 1.05$).

In each iteration, a line search procedure using a second order polynomial fitting (Kemna 2000; Günther 2004) was used to find the optimal step length τ_{opt} between 0 and 1. The model was then updated by $\boldsymbol{m}_{i+1} = \boldsymbol{m}_i + \tau_{\text{opt}}\Delta\boldsymbol{m}_i$. In detail, the full model update was first obtained using eq. (3) for a given model and damping factor. Forward calculations were then carried out for the full update ($\tau = 1$) and half the update ($\tau = 0.5$), and the corresponding total objective function values were then determined. Together with the solution from the previous iteration (i.e. $\tau = 0$), the parameters of the second order polynomial function describing the total objective function as a function of the step length were then obtained. The optimal step length τ_{opt} was then found by searching for the minimum of the parabolic function in the range between $0 < \tau \leq 1$ (Li & Oldenburg 1999; Günther 2004).

The EIT inversion can be implemented with different formulations of the complex data and model parameters, for example the amplitude and phase (Kemna 2000) and the real and imaginary parts of the complex electrical conductivity (Johnson & Thomle 2018). The choice of data and model types is somewhat subjective. In this study, we used the logarithm of both the complex impedances and the complex electrical conductivity as the data and model parameters. The sensitivity for both the real-valued and the complex-valued problems are calculated based on the reciprocity theorem (Geselowitz 1971; Murai & Kagawa 1985; Park & Van 1991). In the complex form, it can be expressed as:

$$\frac{\partial \boldsymbol{Z}^*}{\partial \boldsymbol{\sigma}^*} = -\int \frac{\nabla\phi_{\boldsymbol{C}}^*}{\boldsymbol{I_C}} \cdot \frac{\nabla\phi_{\boldsymbol{P}}^*}{\boldsymbol{I_P}} \mathrm{d}\Omega, \tag{4}$$

where $\phi_{\boldsymbol{C}}^*$ and $\phi_{\boldsymbol{P}}^*$ are the complex potential distribution induced by current excitation $\boldsymbol{I_C}$ and $\boldsymbol{I_P}$ at the transmitter (current poles) and the receiver (potential poles), respectively, dΩ represents a small volume element, and $\boldsymbol{Z}^*$ is the complex transfer impedance, which for a given measurement is the complex potential difference between the potential electrodes normalized by the injected current. The sensitivity for the logarithm of the data and model can be derived using the chain rule:

$$\frac{\partial \ln(\boldsymbol{Z}^*)}{\partial \ln(\boldsymbol{\sigma}^*)} = \frac{\boldsymbol{\sigma}^*}{\boldsymbol{Z}^*}\frac{\partial \boldsymbol{Z}^*}{\partial \boldsymbol{\sigma}^*}. \tag{5}$$

The right-hand side of eq. (5) consists of two different kinds of sensitivity, i.e. the real and imaginary parts of the complex sensitivity. The Cauchy–Riemann conditions describe the relation for the different derivatives (Kwok 2010), that is $\mathrm{Real}\left(\frac{\partial ln(\boldsymbol{Z}^*)}{\partial ln(\boldsymbol{\sigma}^*)}\right) = \frac{\partial ln(|\boldsymbol{Z}^*|)}{\partial ln(|\boldsymbol{\sigma}^*|)} = \frac{\partial \boldsymbol{\varphi_a}}{\partial \boldsymbol{\varphi}}$ and $\mathrm{Imag}\left(\frac{\partial ln(\boldsymbol{Z}^*)}{\partial ln(\boldsymbol{\sigma}^*)}\right) = \frac{\partial \boldsymbol{\varphi_a}}{\partial ln(|\boldsymbol{\sigma}^*|)} = -\frac{\partial ln(|\boldsymbol{Z}^*|)}{\partial \boldsymbol{\varphi}}$ with $\boldsymbol{\varphi}$ and $\boldsymbol{\varphi_a}$ being the phase angle of the complex electrical conductivity and the phase angle of the measured transfer impedance, respectively. The imaginary part of the complex sensitivity (i.e. cross-sensitivity) usually is small compared to the real part of the complex sensitivity, and therefore has been neglected in previous studies (Martin & Günther 2013; Johnson & Thomle 2018).

2.3 Inversion strategies for EIT measurements

2.3.1 Direct complex inversion (CVI)

In principle, the complex impedances can be inverted directly using the inversion scheme described above using the complex form of data and model, that is $\boldsymbol{d} = \ln|\boldsymbol{Z}^*| + i\boldsymbol{\varphi}_a$ and $\boldsymbol{m} = \ln|\boldsymbol{\sigma}^*| + i\boldsymbol{\varphi}$. However, it has been pointed out that the direct inversion of complex data can be problematic for the imaginary part of the model (Kemna 2000; Günther & Martin 2016). The data weighting term in the direct complex inversion is implemented as a complex number (Kemna 2000; Flores Orozco *et al.* 2012b) with the transformed errors for logarithm amplitude as the real part and the errors for the phase as the imaginary part, that is $e = e_A + ie_P$ with e_A and e_P being the data errors for the logarithm of the amplitude and the phase of the measured complex impedance, respectively. This CVI strategy requires the use of complex Jacobian and data weighting matrices and thus the use of the conjugate (Hermitian) transpose, which is typically indicated with H instead of T in eq. (3). In this approach, the complex data misfit was represented by a single real number which is used to stop the inversion, but we will also present the χ^2 values separately for the final electrical conductivity amplitude and phase distributions.

2.3.2 Two-step real-valued inversion (RVI)

The second strategy is a two-step real-valued inversion approach (RVI) based on the Cauchy-Riemann condition for the real part of the sensitivity. It ignores the cross-sensitivity for the inversion of both amplitude and phase of the electrical conductivity. In the first step, the amplitude of the measured complex impedance is inverted using a real-valued formulation, which is identical to ERT inversion. The data and model parameters $\boldsymbol{d}$ and $\boldsymbol{m}$ are the logarithms of the amplitude of the complex impedance $\boldsymbol{ln}(|\boldsymbol{Z}^*|)$ and the electrical conductivity $\boldsymbol{ln}(|\boldsymbol{\sigma}^*|)$. The data weighting term in the first step considers only the log-transformed errors for the amplitude of the measured complex impedances, $e = e_A$. In the second step, the data and model parameters are the measured apparent phase $\boldsymbol{\varphi}_a$ and the phase $\boldsymbol{\varphi}$ for each model element, respectively. The data weighting term only consists of the errors for the phase. The Jacobian matrix from the last iteration in the first step is used in the second step to obtain the model update and to calculate the forward phase response. This is possible because the inverse problem in the second step becomes linear when the cross-sensitivity is ignored (Martin & Günther 2013).

2.3.3 Alternate inversion (ALT)

The third strategy is inspired by the method proposed by Johnson & Thomle (2018), but it should be noted that the decoupled forward calculation approach is not implemented in this study. Instead, we consistently used complex forward computation when it comes to the calculation of complex impedances. In the case of small phase angles below 200 mrad, this method is very similar to the two-step real-valued inversion described above. The first step is again the ERT inversion. The difference is the calculation of the forward responses in the second step. To compare with the approximated forward modelling using the Jacobian matrix in the RVI strategy, we used complex modelling to calculate the forward response in the second step of the ALT strategy. This then becomes the same method as the final phase improvement in Kemna (2000).

The key feature of this strategy is to alternately update the real and imaginary parts of the electrical conductivity in each iteration so that the forward calculation can be carried out based on the updated complex model. To implement this strategy in terms of logarithmic amplitude and phase angle in this study, we calculate the forward response and Jacobian using the exact complex modelling (i.e. eqs 1, 4 and 5), but only the real part of the calculated complex sensitivity will be used to obtain the model update in eq. (3). In particular, the amplitude of complex electrical conductivity is updated first in each iteration. The line search for the amplitude is carried out using polynomial fitting. The complex forward calculation for $\tau = 0.5$ and $\tau = 1$ is based on the phase model from last iteration. The phase model update is then calculated using the same Jacobian and the step length for the phase model is determined using the updated electrical conductivity amplitude. In the end, the forward response, Jacobian matrix and data misfit are updated based on the complex model.

2.3.4 Improved complex inversion (CVI+)

The fourth strategy is an extension of the CVI strategy (CVI+). It also relies on the concept of complex inversion but treats data weighting and model regularization for the amplitude and phase separately. This was achieved by extending the data vector to $\boldsymbol{d} = (\ln(|\boldsymbol{Z}^*|),\ \boldsymbol{\varphi_a})^T$ and the model parameter vector to $\boldsymbol{m} = (\ln(|\boldsymbol{\sigma}^*|),\ \boldsymbol{\varphi}\ )^T$, which are thus twice as large as in the CVI strategy. The data weighting for the amplitude and phase was separately assigned to the corresponding measurements through the diagonal of the extended data weighting matrix. Similarly, an extended regularization matrix was constructed that consists of two original regularization matrices at the main diagonal and two null matrices at the off-diagonal positions. To allow for different regularization strengths for the amplitude and phase, a diagonal matrix $\boldsymbol{L}$ with two separate damping factors is introduced,

$$\boldsymbol{L} = \begin{pmatrix} \lambda_A \boldsymbol{I} & 0 \\ 0 & \lambda_P \boldsymbol{I} \end{pmatrix}, \tag{6}$$

where λ_A and λ_P are the damping factors for the amplitude and phase, respectively. $\boldsymbol{I}$ is the identity matrix. This results in the following modified model update equation

$$\begin{aligned} &\left(\boldsymbol{G}^T \boldsymbol{W}_d^T \boldsymbol{W}_d \boldsymbol{G} + \boldsymbol{W}_m^T \boldsymbol{L} \boldsymbol{W}_m\right) \Delta \boldsymbol{m} \\ &\quad = \boldsymbol{G}^T \boldsymbol{W}_d^T \boldsymbol{W}_d \left(\boldsymbol{d} - f\left(\boldsymbol{m}\right)\right) - \boldsymbol{W}_m^T \boldsymbol{L} \boldsymbol{W}_m \boldsymbol{m} \end{aligned} \tag{7}$$

To complete this extended formulation, the Jacobian matrix is defined as:

$$\boldsymbol{G} = \frac{\partial \boldsymbol{d}}{\partial \boldsymbol{m}} = \begin{pmatrix} \frac{\partial \boldsymbol{ln}(|\boldsymbol{Z}^*|)}{\partial \boldsymbol{ln}(|\boldsymbol{\sigma}^*|)} & \frac{\partial \boldsymbol{ln}(|\boldsymbol{Z}^*|)}{\partial \boldsymbol{\varphi}} \\ \frac{\partial \boldsymbol{\varphi_a}}{\partial \boldsymbol{ln}(|\boldsymbol{\sigma}^*|)} & \frac{\partial \boldsymbol{\varphi_a}}{\partial \boldsymbol{\varphi}} \end{pmatrix} \tag{8}$$

In each iteration, the complex forward operator is required to calculate the forward response and the complex sensitivity which is then used to construct the Jacobian in eq. (8) based on the Cauchy–Riemann relations. The starting damping factors for each term were determined based on the row sums of the matrix product $\boldsymbol{G}^T \boldsymbol{W}_d^T \boldsymbol{W}_d \boldsymbol{G}$ separately using the real part of the complex sensitivity only, which is the same as in the ALT method. The data misfit term for the complete data vector and the separated data misfit terms for amplitude and phase were all examined after each iteration to stop the inversion and to adjust the corresponding damping factors according to the damping scheme of Kemna (2000). At the end of the inversion, it was ensured that the χ^2 values for the extended data vector as well as the separate terms are all in the target range.

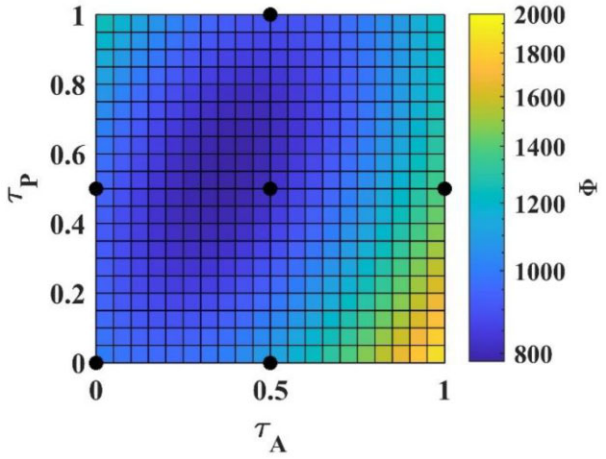

Figure 1. Total objective function value Φ as a function of step lengths τ_A and τ_P for the logarithmic amplitude and phase angle of the electrical conductivity. Values at the six black points are calculated from exact forward modelling to determine the six parameter in eq. (9).

We propose a 2-D line search procedure to find the optimal step lengths τ_A and τ_P for the logarithmic amplitude and phase of the electrical conductivity, respectively. Instead of fitting a three-point polynomial function, we fit a six-point quadratic surface

$$\Phi = \mathrm{A}\tau_A^2 + \mathrm{B}\tau_P^2 + C\tau_A\tau_P + D\tau_A + E\tau_P + F \quad (9)$$

where A-F are the six parameters to determine the quadratic surface. Fig. 1 illustratively shows the 2-D line search method. Once the model update is calculated, forward modelling will be conducted for five combinations of τ_A and τ_P as represented by the black dots in Fig. 1 (i.e. $[\tau_A\ \tau_P] = [0.5\ 0]$, $[0\ 0.5]$, $[0.5\ 0.5]$, $[1\ 0.5]$, $[0.5\ 1]$). Together with the solution from the previous iteration (i.e. $[\tau_A\ \tau_P] = [0\ 0]$), six parameters in eq. (9) can be solved and the minimum of the total functional Φ can be found in the desired range ($0 < \tau_A,\ \tau_P \leq 1$).

2.4 Synthetic modelling study

The two synthetic models shown in Fig. 2 were used in this study. Model-1 has two layers for the amplitude of the electrical conductivity. The top layer has a conductivity of 2 mS m^{-1}, representing a dry soil layer, and the bottom layer has a higher conductivity of 100 mS m^{-1}. The phase distribution shows a phase anomaly with a maximum phase angle of 30 mrad, which could for example represent a target area with zerovalent iron particles (Joyce *et al.* 2012; Emerson *et al.* 2021). In contrast, Model-2 has an extremely high phase angle layer of 1000 mrad, representing highly polarizable materials (e.g. rock salt). Although it is rare in reality, the amplitude of the electrical conductivity for Model-2 is deliberately set as a homogeneous model to illustrate problems with the simplified inversion approaches later on. For both subsurface models, a survey line consisting of 21 electrodes with 1 m electrode spacing and a dipole–dipole measurement scheme were used to obtain the synthetic EIT data. In the synthetic study, we assume that the noise is independent and normally distributed. The modelled complex impedances for Model-1 were contaminated with 3 per cent relative error for the amplitude and 1 mrad absolute error for the phase. For Model-2, 3 per cent relative error for the amplitude was also applied but a higher phase error of 5 mrad was adopted. The applied errors were also used in the subsequent error-weighted inversion. This selection of error parameters is similar to previously used estimates in other studies (Slater & Binley 2006; Martin & Günther 2013; Johnson & Thomle 2018). With this selection of error parameters, it should be noted that all the measurements were equally weighted. This is clear for the phase angle because constant phase errors were applied. For the amplitude of complex impedance, the 3 per cent relative error also corresponds with a constant error after log-transformation (Friedel 2003; Günther *et al.* 2006).

3. RESULTS AND DISCUSSION

3.1 Results for Model-1 (small phase angle)

Fig. 3 shows the inversion results for Model-1 obtained using the four inversion strategies. It should be noted that the results for the RVI and ALT strategies for the amplitude are identical because the implementations have the same first step (i.e. ERT inversion). The results for the inverted electrical conductivity amplitude distribution were very similar for all strategies. The two layers were well reconstructed in all results. Although the data misfit term in the CVI strategy aggregates the data misfit for the amplitude and phase angle in a single real-valued misfit, the χ^2 values are calculated and presented separately for the final electrical conductivity amplitude and phase distributions. The aggregated χ^2 value for the inversion results was minimized to the target range. It was almost identical to χ^2 values of the electrical conductivity amplitude and the ERT inversion result in the first step of the RVI strategy, which indicates that the aggregated misfit in the CVI strategy was dominated by the error for the electrical conductivity amplitude as expected. The inverted phase distribution obtained with the CVI strategy was rough and showed artefacts. The high phase anomaly was not accurately located and the overall image appeared very rough, although the final χ^2 value of the phase inversion obtained with the CVI strategy was very close to the target range. In contrast, the phase anomaly was well resolved in the distributions obtained using the RVI, ALT and CVI + strategies. Moreover, the images were very similar and presented much smoother phase distributions. It should be noted that the χ^2 value for the phase distribution obtained using the RVI strategy is calculated with the forward response approximated using the Jacobian matrix. We also calculated the exact χ^2 value using a complex modelling, and the result was 1.086 instead of the 1.041 using the approximated Jacobian matrix. Although it is slightly higher than the upper limit of the target range, it is still acceptable.

From the imaging results presented in Fig. 3, it is clear that visible differences can only be found in the phase images produced by the CVI strategy. This is due to the use of the same data weighting and damping factor for the amplitude and the phase angle in the CVI strategy. However, the appropriate regularization strength and thus the optimal damping factor can be quite different for the inversion of electrical conductivity amplitude and phase angle. Table 1 presents the data weighting and final damping factors for the inversion of phase angle using different strategies. Because both the inversion of electrical conductivity amplitude and phase angle are equal-weighted inversions in this synthetic study, we can use one value (i.e. $|1/e|^2$ in Table 1) to represent the data weighting. The RVI, ALT and CVI + strategies have the same data weighting and comparable damping factors for the inversion of the phase angle because these strategies allow for separated treatment of the amplitude and phase angle in terms of data weighting and model regularization. For the CVI strategy, the data weighting and final damping factor were quite different from the other strategies. In principle, the CVI

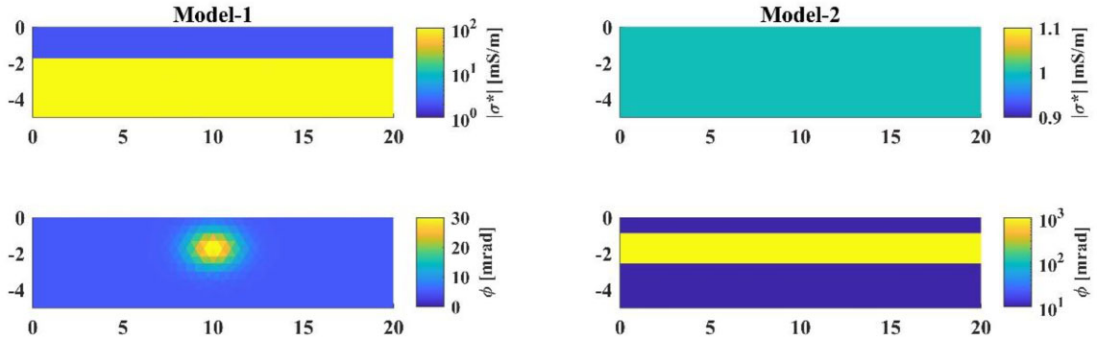

Figure 2. Amplitude and phase of two subsurface models used in the synthetic modelling study.

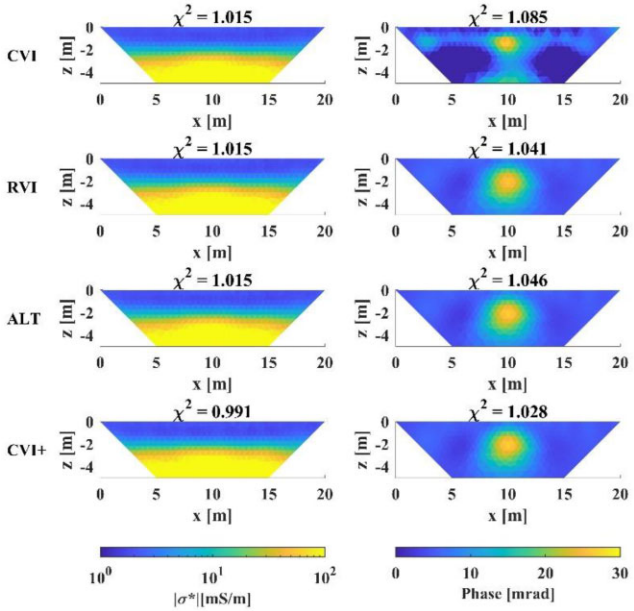

Figure 3. Inversion results for electrical conductivity amplitude and phase of Model-1 using the CVI (direct complex inversion), RVI (two-step real-valued inversion), ALT (alternate inversion or final phase improvement) and CVI + (improved complex inversion) strategies.

Table 1. Data weighting and the final damping factors for different inversion strategies in the inversion of the phase angle of Model-1.

Method	$\lvert 1/e\rvert^2$	Final damping factor λ	$\frac{\lambda}{\lvert 1/e\rvert^2}$
CVI	1.11×10^3	6.63×10^1	0.06
RVI	1.00×10^6	1.63×10^6	1.63
ALT	1.00×10^6	1.64×10^6	1.64
CVI+	1.00×10^6	1.42×10^6	1.42

strategy should be able to provide a plausible phase distribution if the ratio of the final damping factor and the data weighting would be similar as in the other strategies. However, Table 1 shows that this ratio was much smaller (0.06 compared to 1.63), indicating that the rough phase images produced by the CVI strategy are due to the smaller regularization strength applied in the phase inversion. This fundamentally explains why the direct complex inversion (CVI) is not able to produce reliable inversion results for the phase angle. Depending on the different contrasts in the amplitude and phase of the electrical conductivity distribution and different data errors in the measured amplitude and phase of the complex impedances, the phase model can be under- or overestimated. Kemna (2000) proposed a final phase improvement starting from the phase model obtained using the direct complex inversion, which was useful given that the cases presented in Kemna (2000) were underestimated or slightly overestimated. The rough phase model with artefacts shown in Fig. 3 may not be a good starting model for a second phase inversion step. Therefore, it is suggested that such a second step should start from a homogeneous model as in the RVI and ALT strategies.

The results produced by the CVI + strategy show slightly different final χ^2 values and damping factors compared to the RVI and ALT strategies. This is because the use of the two-dimensional line search can result in different step lengths and thus different damping of λ. Moreover, the starting λ for the inversion of the phase angle in the CVI + strategy is estimated based on the Jacobian calculated using a homogeneous model, while the starting λ for the phase angle in the RVI and ALT strategies is estimated based on the Jacobian for the final electrical conductivity model. Despite these differences, the final χ^2 values for the RVI, ALT, and CVI + strategies were all in the target range and the final damping factors were similar and of the same order of magnitude.

3.2 Results of Model-2 (large phase model)

Fig. 4 shows the inversion results for Model-2 obtained using the four inversion strategies. It is clear that only the CVI + strategy successfully resolved the homogeneous amplitude of the electrical conductivity model, whereas the other strategies all resulted in anomalies in the inverted amplitude of the electrical conductivity. Although the phase distributions obtained by the CVI, RVI and ALT strategies clearly showed the layered structure, it is difficult to interpret without a reliable distribution of the amplitude of the electrical conductivity. Therefore, the results obtained by the CVI + strategy were considered as a reference and the reasons for the failure of the other three strategies will be explained in the following.

In the case of Model-1, the inversion results produced by the CVI strategy were dominated by the real part of the data and the model. However, this is not the case anymore in the presence of extremely large phase angles (i.e. Model-2). To analyse the inversion results of Model-2 produced by the CVI strategy and to compare them with the results produced by the CVI + strategy, the data weighting and the final damping factors for the CVI and CVI + strategy are presented in Table 2. The ratio of the final damping factor and the data weighting for the CVI strategy was about two orders of magnitude smaller (0.05 compared to 7.05) than the ratio for the CVI + strategy in case of the inversion of the amplitude of the impedance. This indicates that the regularization strength applied to the amplitude was too small in the CVI strategy. In the case of the inversion of the phase angle, the difference in the ratios for

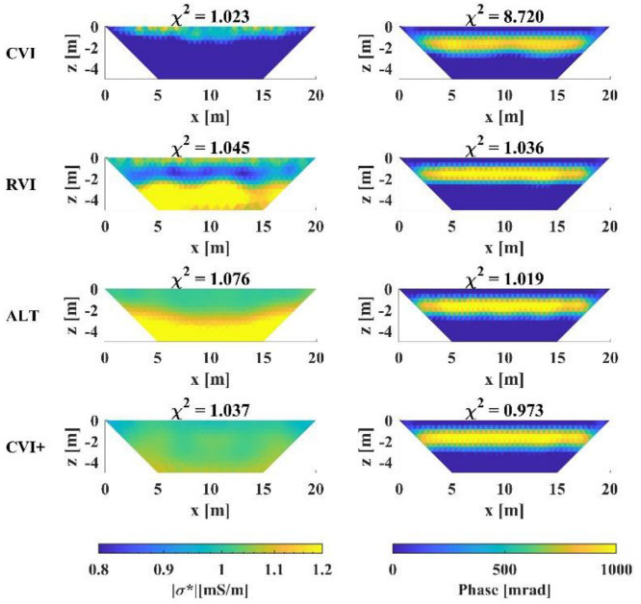

Figure 4. Inversion results for electrical conductivity amplitude and phase of Model-2 using CVI (direct complex inversion), RVI (two-step real-valued inversion), ALT (alternate inversion or final phase improvement) and CVI+ (improved complex inversion) strategies.

Table 2. Data weighting and the final damping factors for the CVI and CVI + strategies in the inversion of Model-2.

Method		$\lvert 1/e\rvert^2$	Final damping factor λ	$\frac{\lambda}{\lvert 1/e\rvert^2}$
Amplitude	CVI	1.11×10^3	5.95×10^1	0.05
	CVI+	1.14×10^3	8.04×10^3	7.05
Phase	CVI	1.11×10^3	5.95×10^1	0.05
	CVI+	4.00×10^4	3.58×10^2	0.009

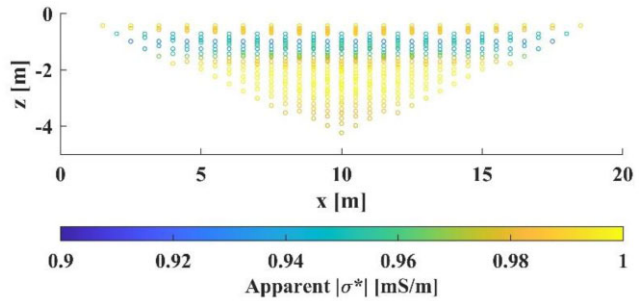

Figure 5. Pseudo-section of the amplitude of the modelled apparent complex conductivity using Model-2

the CVI and CVI + strategies were much smaller, which suggests that the inversion results for Model-2 obtained by the CVI strategy were dominated by the phase angle and not the amplitude. Although the final χ^2 value for the amplitude of the electrical conductivity was in the target range for the CVI strategy, the image presented mostly lower electrical conductivity (<0.8 mS m^{-1}), which is much different from the expected homogeneous distribution of 1 mS m^{-1}.

The inversion results obtained by the RVI strategy showed a layered structure for the amplitude of the electrical conductivity, which is not in agreement with the homogeneous true model. The reason for the failure of the RVI strategy is rooted in the modelled amplitude of the apparent conductivity. Fig. 5 shows the pseudo-section of the amplitude of the modelled apparent electrical conductivity using Model-2, which clearly showed a relatively low conductivity layer in the middle. This explains the layered structure obtained for the inverted amplitude of the complex conductivity using the RVI strategy. In the case of ERT or EIT with small phase values, the modelled apparent electrical conductivity for a homogeneous conductivity amplitude of 1 mS m^{-1} is expected to be 1 mS m^{-1}. Due to the extremely large phase angles, the amplitude of the modelled apparent electrical conductivity ranges from 0.92 to 1.02, which suggest differences up to 8 per cent. The final χ^2 values for the results obtained by the RVI strategy were also calculated using a complex instead of the real-valued forward modelling, and this resulted in χ^2 values of 114.16 and 787.86 for the amplitude and phase, respectively. This clearly highlights that in the case of large phase angles the RVI strategy is not suitable for the inversion of EIT data and that complex forward modelling is needed. Although the ALT strategy can produce accurate forward responses, the result obtained with the ALT strategy were also not satisfactory. The reason for this failure of the ALT strategy is the negligence of the cross-sensitvity, which will be explained in detail in the next section.

3.3 Discussion of cross-sensitivity

To explore how the cross-sensitivity contributes to the inversion of the amplitude and phase angle of the electrical conductivity, four different Jacobian matrices were defined based on the complete extended Jacobian in eq. (8):

$$\boldsymbol{G}_{A0} = \frac{\partial \boldsymbol{ln}\left(|\boldsymbol{Z}^*|\right)}{\partial \boldsymbol{ln}\left(|\boldsymbol{\sigma}^*|\right)},\ \boldsymbol{G}_{AX} = \begin{pmatrix} \frac{\partial \boldsymbol{ln}\left(|\boldsymbol{Z}^*|\right)}{\partial \boldsymbol{ln}\left(|\boldsymbol{\sigma}^*|\right)} \\ \frac{\partial \boldsymbol{\varphi}_a}{\partial \boldsymbol{ln}\left(|\boldsymbol{\sigma}^*|\right)} \end{pmatrix},$$

$$\boldsymbol{G}_{P0} = \frac{\partial \boldsymbol{\varphi}_a}{\partial \boldsymbol{\varphi}},\ \boldsymbol{G}_{PX} = \begin{pmatrix} \frac{\partial \boldsymbol{ln}\left(|\boldsymbol{Z}^*|\right)}{\partial \boldsymbol{\varphi}} \\ \frac{\partial \boldsymbol{\varphi}_a}{\partial \boldsymbol{\varphi}} \end{pmatrix} \tag{9}$$

where $\boldsymbol{G}_{A0}$ and $\boldsymbol{G}_{P0}$ represent the Jacobian for the logarithmic of the conductivity amplitude and the phase angle without considering the cross-sensitivity (i.e. the real part of the sensitivity and $\boldsymbol{G}_{A0} = \boldsymbol{G}_{P0}$), and $\boldsymbol{G}_{AX}$ and $\boldsymbol{G}_{PX}$ represent the Jacobian for the logarithmic of the conductivity amplitude and the phase angle including the cross-sensitivity.

The inversion results of Model-2 obtained with the ALT and CVI + strategy indicated that the cross-sensitivity provided unique information during the inversion. To evaluate the information content in the Jacobian matrix, the relative eigenvalue range (RER) of the Hessian matrix ($\boldsymbol{H} = \boldsymbol{G}^T \boldsymbol{W}_d^T \boldsymbol{W}_d \boldsymbol{G}$) was adopted (see Appendix A for more information). In short, the RER value represents the resolved model space and high RER values correspond to a small null space in the model space. The calculated complex sensitivity of the model obtained in the first iteration was adopted for the determination of the RER value because the cross-sensitivity for the homogeneous start model is zero. It should also be noted that the eigenvalue spectra for the amplitude and phase angle should be identical in the absence of data weighting, but can be different when data weighting is considered. Fig. 6 presents the eigenvalue spectra of different Jacobian matrices for both Model-1 and Model-2. In the case of Model-1, the RER values of the Jacobian matrices $\boldsymbol{G}_{A0}$ and $\boldsymbol{G}_{AX}$ at the selected damping level (Fig. 6a) as well as the RER values for the spectra of $\boldsymbol{G}_{P0}$ and $\boldsymbol{G}_{PX}$ (Fig. 6b) are identical. This explains why the negligence of the cross-sensitivity has no effect on the results of Model-1. In the case of Model-2, the RER values of the Jacobian matrices $\boldsymbol{G}_{A0}$ and $\boldsymbol{G}_{AX}$ at the selected damping level (Fig. 6c) showed considerable differences. The RER value of $\boldsymbol{G}_{AX}$ was about 1.5 times larger than the RER value of $\boldsymbol{G}_{A0}$, which

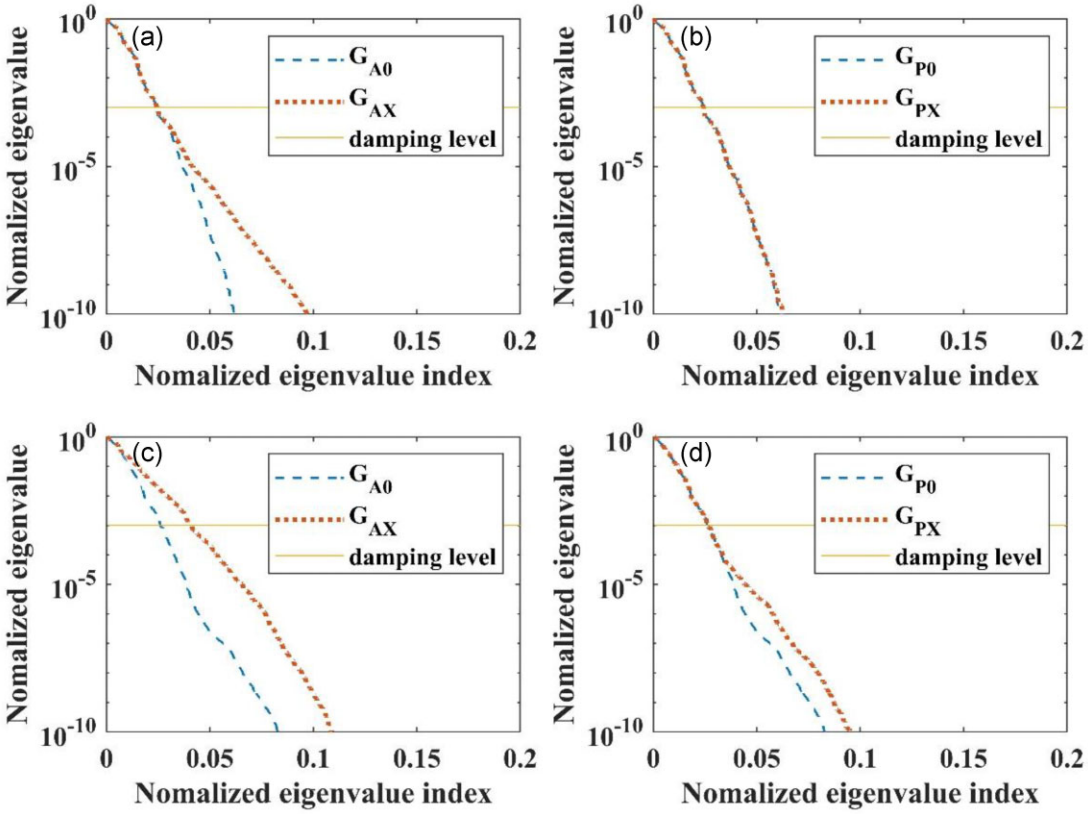

Figure 6. Eigenvalue spectrums of the different Jacobians for the amplitude (a) and phase (b) of electrical conductivity for Model-1 and the amplitude (c) and phase (d) of electrical conductivity for Model-2.

indicates that the information in the cross-sensitivity contributed significantly to the inversion of the electrical conductivity amplitude. Fig. 6(d) shows that the RER values of the Jacobian matrices $\boldsymbol{G}_{P0}$ and $\boldsymbol{G}_{PX}$ for Model-2 were identical. However, the calculation of $\boldsymbol{G}_{P0}$ also requires a reliable model for the electrical conductivity amplitude, which in the case of large phase angle can only be obtained by considering both the real part of the sensitivity and the cross-sensitivity in the inversion.

Finally, we analyse the model update calculated using the Jacobian with and without cross-sensitivity. The model update considering the cross-sensitivity was obtained using the CVI + strategy. The model update calculated without cross-sensitivity was also based on the CVI + formulation, but the off-diagonal positions in the extended Jacobian matrix were set to zero. Fig. 7(a) shows the amplitude of the electrical conductivity obtained using the CVI + strategy in the first iteration. Although the calculation was based on the logarithmic model parameter, we present the results in the linear space to be consistent with the presentation of the true model. The electrical conductivity distribution in Fig. 7(a) shows that a slightly higher conductivity layer starts to appear in the image. Figs 7(b) and (c) present the calculated model update in the second iteration without and with the consideration of the cross-sensitivity, respectively. The model update calculated without cross-sensitivity tends to enhance the conductive layer that appeared in the first iteration, which leads the model far from a homogeneous distribution for the electrical conductivity amplitude. In contrast, the model update calculated with cross-sensitivity updates the model towards a homogenous distribution. This highlights the unique contribution of the cross-sensitivity during the inversion.

4. CONCLUSIONS AND OUTLOOK

In this study, we presented detailed formulations of four different inversion strategies for EIT measurements. The first strategy (CVI) is a complex-valued approach that follows the formulation for ERT inversion but the parameters are all complex. The second strategy (RVI) is a two-step real-valued approach where the amplitude of data is inverted first in the real number domain using the ERT inversion routine, and the phase is then separately inverted using the final real-valued Jacobian from the first step. In case of small phase values, the third strategy (ALT) is similar to the two-step RVI approach but considers complex forward modelling in the second step. In the case of large phase values, the ALT strategy updates the real and imaginary parts of the model alternately so that the real part of the forward response can also be calculated based on the complex model. The fourth strategy (CVI+) is a newly formulated complex approach. Instead of using complex data and model vectors, the CVI + strategy separates the real and imaging part of the data and model vectors, which allows to consider the complex coupling while allowing separate data weighting and model regularization for the real and imaginary parts.

We tested the different inversion strategies using two synthetic models. Model-1 represents an environmental application with small phase angles. The inverted amplitude of the electrical conductivity showed comparable images with the true model for all strategies. The inverted phase distribution obtained by the CVI strategy showed anomalies, while the inverted phase distributions obtained by the RVI, ALT and CVI + strategies were similar and in good agreement with the true model. The rough phase model obtained by the CVI strategy was attributed to the domination of the real part of

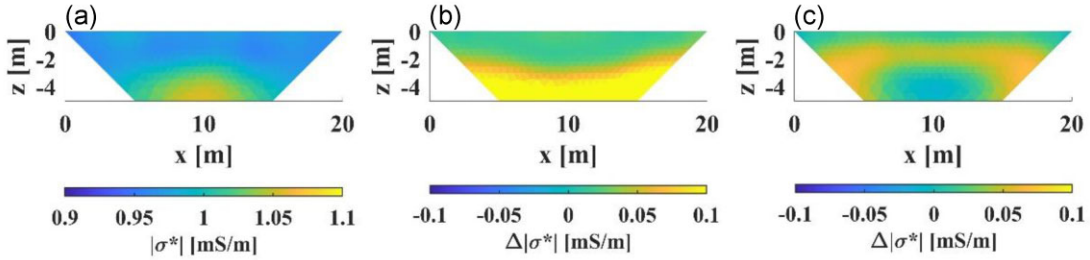

Figure 7. (a) Electrical conductivity amplitude obtained using CVI + in the first iteration, (b) calculated model update without consideration of cross-sensitivity and (c) calculated model update with consideration of cross-sensitivity.

the data and model in the inversion, which results in much smaller regularization strength for the inversion of the phase angle. It was concluded that the RVI, ALT and CVI + strategies were all able to provide reliable inversion results in the absence of small measured phase values.

The performance of the four inversion strategies in the presence of high phase values was evaluated using Model-2, which has extremely large phase angles. For this model, only the CVI + strategy produced plausible inversion results that were in good agreement with the true model. The reason for the failure of the CVI strategy was again related to the aggregated formulation, although the objective function was dominated by the phase angle in the case of Model-2. The failure of the RVI strategy was attributed to errors in the amplitude of the modelled data when not considering complex forward modelling, which was visualized and clearly explained by the pseudo-section of the amplitude of the modelled electrical conductivity. The ALT strategy also failed to produce reliable inversion results in the case of Model-2, which was attributed to the negligence of the cross-sensitivity in the inversion. The relative eigenvalue range was used to evaluate the information content provided by the cross-sensitivity. It was found that the RER value of the Jacobian considering the cross-sensitivity was much higher compared to the Jacobian without cross-sensitivity in the inversion of the amplitude of complex impedances, which indicates that the cross-sensitivity provided unique information in the inversion. This was supported by the calculated model update using different Jacobian matrices. It should be noted that the RVI strategy has its practical advantage that no complex calculations are required, which substantially reduces the computation load. Therefore, it can be concluded that the CVI + strategy is theoretically the most comprehensive and correct approach for EIT data inversion, but that in the case of small phase angles the RVI strategy should be preferred given its fast calculation and low storage requirement.

Two directions can be identified for further testing and improvement of EIT data inversion. One is to test the different inversion strategies with field measurements. We tested with two typical measurements that have small phase angles and the results (presented in Appendix B) were similar to what has been presented for Model-1. However, for measurements with extremely large phase angles, the different strategies need to be tested in the future. The other direction could be the investigation of different data and model types instead of the amplitude and phase considered here (e.g. the real and imaginary part). There is no clear guideline for the choice of data and model types in the inversion of EIT data, and the use of different data and model types is somewhat subjective depending on the preferred interpretation of the results. Therefore, a comparison of different data and model types in the EIT data inversion should be conducted in the future with a proper error transformation model for different data types.

ACKNOWLEDGMENTS

Haoran Wang would like to thank the China Scholarship Council for funding this research. This work has also partially been funded by the Deutsche Forschungsgemeinschaft (DFG, German Research Foundation) under Germany's Excellence Strategy, EXC-2070–390732324–PhenoRob. We appreciate reviews and comments by Deqiang Mao and Tim Johnson.

DATA AVAILABILITY

The data supporting the findings of this study are available upon reasonable request.

CONFLICT OF INTEREST

The authors declare that they have no conflict of interest.

REFERENCES

Attwa, M. & Günther, T., 2013. Spectral induced polarization measurements for predicting the hydraulic conductivity in sandy aquifers, *Hydrol. Earth Syst. Sci.,* **17**(10), 4079–4094.

Beard, L.P., Hohmann, G.W. & Tripp, A.C., 1996. Fast resistivity IP inversion using a low-contrast approximation, *Geophysics,* **61**(1), 169–179.

Blome, M., Maurer, H. & Greenhalgh, S., 2011. Geoelectric experimental design - efficient acquisition and exploitation of complete pole-bipole data sets, *Geophysics,* **76**(1), F15–F26.

Bücker, M. & Hördt, A., 2013. Analytical modelling of membrane polarization with explicit parametrization of pore radii and the electrical double layer, *Geophys. J. Int.,* **194**(2), 804–813.

Cai, G.C., Vanderborght, J., Klotzsche, A., van der Kruk, J., Neumann, J., Hermes, N. & Vereecken, H., 2016. Construction of minirhizotron facilities for investigating root zone processes, *Vadose Zone J.,* **15**(9), 1–13.

Chou, T.-K., Chouteau, M. & Dube, J.-S., 2016. Intelligent meshing technique for 2D resistivity inverse problems, *Geophysics,* **81**(4), IM45–IM56.

Dahlin, T. & Leroux, V., 2012. Improvement in time-domain induced polarization data quality with multi-electrode systems by separating current and potential cables, *Near Surf. Geophys.,* **10**(6), 545–565.

Dey, A. & Morrison, H.F., 1979. Resistivity modeling for arbitrarily shaped 2-dimensional structures, *Geophys. Prospect.,* **27**(1), 106–136.

Doetsch, J., Fiandaca, G., Auken, E., Christiansen, A.V., Cahill, A.G. & Jakobsen, R., 2015. Field-scale time-domain spectral induced polarization monitoring of geochemical changes induced by injected CO_2 in a shallow aquifer, *Geophysics,* **80**(2), WA113–WA126.

Emerson, H.P. *et al.*, 2021. *Spectral Induced Polarization-biogeochemical Relationships for Remediation Amendment Monitoring*. Technical Report, Prepared for the U.S. Department of Energy under Contract DE-AC05-76RL01830. Retrieved from: https://www.osti.gov/biblio/1835069 https://www.osti.gov/servlets/purl/1835069.

Farquharson, C.G. & Oldenburg, D.W., 2004. A comparison of automatic techniques for estimating the regularization parameter in non-linear inverse problems, *Geophys. J. Int.,* **156**(3), 411–425.

Flores Orozco, A., Aigner, L. & Gallistl, J., 2021. Investigation of cable effects in spectral induced polarization imaging at the field scale using multicore and coaxial cables, *Geophysics,* **86**(1), E59–E75.

Flores Orozco, A., Kemna, A., Oberdoerster, C., Zschornack, L., Leven, C., Dietrich, P. & Weiss, H., 2012a. Delineation of subsurface hydrocarbon contamination at a former hydrogenation plant using spectral induced polarization imaging, *J. Contam. Hydrol.,* **136,** 131–144.

Flores Orozco, A., Kemna, A. & Zimmermann, E., 2012b. Data error quantification in spectral induced polarization imaging, *Geophysics,* **77**(3), E227–E237.

Friedel, S., 2003. Resolution, stability and efficiency of resistivity tomography estimated from a generalized inverse approach, *Geophys. J. Int.,* **153**(2), 305–316.

Geselowitz, D.B., 1971. Application of electrocardiographic lead theory to impedance plethysmography, *IEEE Trans. Biomed. Eng.,* **BM18**(1), 38–41.

Geuzaine, C. & Remacle, J.-F., 2009. Gmsh: a 3-D finite element mesh generator with built-in pre- and post-processing facilities, *Int. J. Numer. Methods Eng.,* **79**(11), 1309–1331.

Günther, T., 2004. Inversion methods and resolution analysis for the 2D/3D reconstruction of resistivity structures from Dc measurements, *PhD thesis*, Universitätsbibliothek der TU BAF.

Günther, T. & Martin, T., 2016. Spectral two-dimensional inversion of frequency-domain induced polarization data from a mining slag heap, *J. Appl. Geophys.,* **135,** 436–448.

Günther, T., Rücker, C. & Spitzer, K., 2006. Three-dimensional modelling and inversion of dc resistivity data incorporating topography - II. Inversion, *Geophys. J. Int.,* **166**(2), 506–517.

Inzoli, S., 2016. Experimental and statistical methods to improve the reliability of spectral induced polarization to infer litho-textural properties of alluvial sediments, *PhD thesis*, Università degli Studi di Milano, Italy. https://hdl.handle.net/2434/360596.

Johnson, T.C. & Thomle, J., 2018. 3-D decoupled inversion of complex conductivity data in the real number domain, *Geophys. J. Int.,* **212**(1), 284–296.

Joyce, R.A., Glaser, D.R., Werkema, D.D. & Atekwana, E.A., 2012. Spectral induced polarization response to nanoparticles in a saturated sand matrix, *J. appl. Geophys.,* **77,** 63–71.

Kemna, A., 2000. *Tomographic Inversion of Complex Resistivity,* Ruhr-Universität Bochum.

Koestel, J., Kemna, A., Javaux, M., Binley, A. & Vereecken, H., 2008. Quantitative imaging of solute transport in an unsaturated and undisturbed soil monolith with 3-D ERT and TDR, *Water Resour. Res.,* **44**(12), 10.1029/2007wr006755.

Krampe, V., Edme, P. & Maurer, H., 2021. Optimized experimental design for seismic full waveform inversion: a computationally efficient method including a flexible implementation of acquisition costs, *Geophys. Prospect.,* **69**(1), 152–166.

Kulenkampff, J.M. & Yaramanci, U., 1993. Frequency-dependent complex resistivity of rock-salt samples and related petrophysical parameters, *Geophys. Prospect.,* **41**(8), 995–1008.

Kwok, Y.K., 2010. *Applied Complex Variables for Scientists and Engineers,* Cambridge Univ. Press.

LaBrecque, D.J., Miletto, M., Daily, W., Ramirez, A. & Owen, E., 1996. The effects of noise on Occam's inversion of resistivity tomography data, *Geophysics,* **61**(2), 538–548.

Li, Y. & Oldenburg, D.W., 1999. 3-D inversion of DC resistivity data using an L-curve criterion, in *SEG Technical Program Expanded Abstracts 1999,* pp. 251–254, Society of Exploration Geophysicists.

Loke, M.H. & Barker, R.D., 1996. Rapid least-squares inversion of apparent resistivity pseudosections by a quasi-Newton method, *Geophys. Prospect.,* **44**(1), 131–152.

Martin, T. & Günther, T., 2013. Complex resistivity tomography (CRT) for fungus detection on standing oak trees, *Eur. J. Forest Res.,* **132**(5-6), 765–776.

Maurer, H., Greenhalgh, S. & Latzel, S., 2009. Frequency and spatial sampling strategies for crosshole seismic waveform spectral inversion experiments, *Geophysics,* **74**(6), WCC79–WCC89.

Maurya, P.K., Balbarini, N., Moller, I., Ronde, V., Christiansen, A.V., Bjerg, P.L., Auken, E. & Fiandaca, G., 2018. Subsurface imaging of water electrical conductivity, hydraulic permeability and lithology at contaminated sites by induced polarization, *Geophys. J. Int.,* **213**(2), 770–785.

Murai, T. & Kagawa, Y., 1985. Electrical-impedance computed-tomography based on a finite-element model, *IEEE Trans. Biomed. Eng.,* **32**(3), 177–184.

Oldenburg, D.W. & Li, Y.G., 1994. Inversion of induced polarization data, *Geophysics,* **59**(9), 1327–1341.

Park, S.K. & Van, G.P., 1991. Inversion of pole-pole data for 3-d resistivity structure beneath arrays of electrodes, *Geophysics,* **56**(7), 951–960.

Peruzzo, L. *et al.*, 2021. Three-channel electrical impedance spectroscopy for field-scale root phenotyping, *Plant Phenom. J.,* **4**(1), e20021.

Radic, T., 2004. Elimination of cable effects while multi-channel sip measurements, in *Paper presented at the Near Surface 2004-10th EAGE European Meeting of Environmental and Engineering Geophysics,* 06–09 September 2004, Utrecht, Netherlands.

Revil, A. *et al.*, 2017. Complex conductivity of soils, *Water Resour. Res.,* **53**(8), 7121–7147.

Revil, A. & Florsch, N., 2010. Determination of permeability from spectral induced polarization in granular media, *Geophys. J. Int.,* **181**(3), 1480–1498.

Sasaki, Y., 1992. Resolution of resistivity tomography inferred from numerical-simulation, *Geophys. Prospect.,* **40**(4), 453–463.

Schmutz, M., Ghorbani, A., Vaudelet, P. & Blondel, A., 2014. Cable arrangement to reduce electromagnetic coupling effects in spectral-induced polarization studies, *Geophysics,* **79**(2), A1–A5.

Slater, L. & Binley, A., 2006. Synthetic and field-based electrical imaging of a zerovalent iron barrier: implications for monitoring long-term barrier performance, *Geophysics,* **71**(5), B129–B137.

Vogel, C.R., 2002. *Computational Methods for Inverse Problems,* Society for Industrial and Applied Mathematics.

Wang, H., Huisman, J.A., Zimmermann, E. & Vereecken, H., 2021. Experimental design to reduce inductive coupling in spectral electrical impedance tomography (SEIT) measurements, *Geophys. J. Int.,* **225**(1), 222–235. https://doi.org/10.1093/gji/ggaa594.

Wang, H., Lin, C.P., Mok, T.H., Wu, P.L. & Liu, H.C., 2022. High-fidelity subsurface resistivity imaging incorporating borehole measurements for monitoring underground construction, *Eng. Geol.,* **299,** doi:10.1016/j.enggeo.2022.106558.

Weigand, M. & Kemna, A., 2019. Imaging and functional characterization of crop root systems using spectroscopic electrical impedance measurements, *Plant Soil,* **435**(1-2), 201–224.

Weigand, M., Zimmermann, E., Michels, V., Huisman, J.A. & Kemna, A., 2022. Design and operation of a long-term monitoring system for spectral electrical impedance tomography (SEIT), *Geosci. Instrum. Method. Data Syst. Discuss.,* **2022,** 1–35. https://doi.org/10.5194/gi-11-413-2022.

Weihermüller, L., Huisman, J.A., Lambot, S., Herbst, M. & Vereecken, H., 2007. Mapping the spatial variation of soil water content at the field scale with different ground penetrating radar techniques, *J. Hydrol.,* **340**(3-4), 205–216.

Weller, A., Gruhne, M., Seichter, M. & Borner, F.D., 1996a. Monitoring hydraulic experiments by complex conductivity tomography, *Eur. J. Environ. Eng. Geophys.,* **1,** 209–228. https://doi.org/10.4133/1.2922452.

Weller, A., Seichter, M. & Kampke, A., 1996b. Induced-polarization modelling using complex electrical conductivities, *Geophys. J. Int.,* **127**(2), 387–398.

Xu, B.W. & Noel, M.. 1993. On the completeness of data sets with multielectrode systems for electrical-resistivity survey, *Geophys. Prospect.,* **41**(6), 791–801. https://doi.org/10.1111/j.1365-2478.1993.tb00885.x.

Zhao, Y., Zimmermann, E., Huisman, J.A., Treichel, A., Wolters, B., van Waasen, S. & Kemna, A., 2015. Phase correction of electromagnetic coupling effects in cross-borehole eit measurements, *Meas. Sci. Technol.,* **26**(1), 015801.

Zimmermann, E., 2011. Phasengenaue Impedanzspektroskopie und -tomographie für Geophysikalische Anwendungen, *PhD thesis*, Rheinischen Friedrich-Wilhelms-Universität Bonn. https://bonnus.ulb.uni-bonn.de/permalink/49HBZ_ULB/idtnkp/alma991040864679706467.

Zimmermann, E., Huisman, J., Kemna, A., Berwix, J., Glaas, W., Meier, H., Wolters, B. & Esser, O., 2010. Advanced electrical impedance tomography system with high phase accuracy, in *Paper Presented at the Proceedings of the 6th World Congress on Industrial Process Tomography (WCIPT6),* Beijing, China. https://www.isipt.org/world-congress/6/717.html.

Zimmermann, E., Huisman, J.A., Mester, A. & van Waasen, S., 2019. Correction of phase errors due to leakage currents in wideband eit field measurements on soil and sediments, *Meas. Sci. Technol.,* **30**(8), doi:10.1088/1361-6501/ab1b09.

Zimmermann, E., Kemna, A., Berwix, J., Glaas, W. & Vereecken, H., 2008. Eit measurement system with high phase accuracy for the imaging of spectral induced polarization properties of soils and sediments, *Meas. Sci. Technol.,* **19**(9), doi:10.1088/0957-0233/19/9/094010.

APPENDIX A: EIGENVALUE SPECTRUM OF HESSIAN MATRIX

Fig. A1 shows a typical eigenvalue spectrum of the Hessian matrix. The calculated eigenvalues are normalized by the largest eigenvalue, and the indices of the eigenvalues are normalized by the total number of model parameters. A threshold value of the damping level should be defined to separate the resolved model space and the null space. As defined in Maurer *et al.* (2009), the part to the left of the intersection of the spectrum with the threshold line is considered as the relative eigenvalue range (RER) and the remaining part of the spectrum is the null space. The RER has been used in optimized experimental design for seismic full waveform inversion (Maurer *et al.* 2009; Krampe *et al.* 2021) and in the assessment of geoelectrical measurement configurations (Blome *et al.* 2011; Wang *et al.* 2022). The choice of damping level is subjective and survey dependent as pointed out in Krampe *et al.* (2021). A threshold value of 10^{-3} as used in Blome *et al.* (2011) and Wang *et al.* (2022) for the ERT problem was adopted in this study.

APPENDIX B: INVERSION RESULTS OF FIELD MEASUREMENTS

In addition to the synthetic modelling study, two field data sets were also tested to compare the inversion strategies. The first data set was acquired in a kaolinite quarry in Lozzolo, Italy, which has been already used in Zimmermann *et al.* (2019) and Wang *et al.* (2021). For more information about this site, we refer to Inzoli (2016). The survey line has 30 electrodes with 1 m electrode spacing. The measurement scheme followed a circulating strategy (Xu & Noel 1993) where 16 electrodes were skipped between the two current poles for each injection. The same skip was also applied to the final four-pole data to obtain normal and reciprocal measurements. The data used in this study was measured at 6 Hz where electromagnetic coupling effects can be neglected (Zimmermann *et al.* 2019). The data error was estimated from the normal and reciprocal measurements using a multibin approach (Koestel *et al.* 2008) to fit the error models proposed by Flores Orozco *et al.* (2012b). The second field data set was measured in Selhausen, Germany (Weigand *et al.* 2022). The soil at this site is a Luvisol that developed in a layer with a silt loam texture (Weihermüller *et al.* 2007; Cai *et al.* 2016). The data was measured using a long-term EIT monitoring system which has 40 electrodes with 25 cm spacing. The selected electrode configurations (647 data points) were adapted to the capabilities of the multichannel system while still providing enough information of the subsurface. The presented data from the Selhausen site was measured at 1 Hz where the electromagnetic coupling effects can be neglected. The data error for the Selhausen data set follows the analysis of Weigand *et al.* (2022), who determined error estimates based on a systematic parameter search. For more information about the data sets and the choice of error parameters, we refer to Weigand *et al.* (2022).

Fig. B1 shows the inversion results for the Lozzolo data set. The inverted electrical conductivity amplitudes obtained with the four inversion strategies were again very similar with conductivity values mostly between 2 and 50 mS m^{-1}. Similar patterns could be observed in the inverted phase distributions. There was a weakly polarized layer near the surface and higher phase angles around 20 mrad appeared below this first layer. The inverted phase distribution obtained by the CVI method was again rougher than the other distributions and presented minor artefacts near the surface, which is again due to the damping factor as in the synthetic modelling study. Fig. B2 shows the inversion results for the Selhausen data set. The inverted electrical conductivity amplitude presented a very thin layer at the top with low conductivity, while the overall electrical conductivity values were at a high level of about 100 mS m^{-1}. As in the previous examples, the inversion results for the electrical conductivity amplitude were similar for all inversion strategies. The inverted phase distributions produced by the RVI, ALT and CVI + strategies were smooth and similar, while the phase distribution obtained by the CVI strategy showed erratic high and low phase values extensively in the profile. This is because the applied damping factor in the CVI approach is much smaller compared to the synthetic cases and the Lozzolo data set. If the mean value of the individual data weighting is used to represent the data weighting term, this is further supported by the ratio of the final damping factor and the data weighting as in the synthetic study. This ratio was only two orders of magnitude smaller for the CVI strategy than the other two strategies for the Lozzolo data set, which explains why the observed differences between the three strategies were relatively small. The ratio was four orders of magnitude smaller for the Selhausen data set, which explains the erratic inversion results for the phase distribution.

Both field examples are in agreement with the conclusions obtained from the synthetic model study with Model-1. However, the electrode configurations used in the two field examples were different from the conventional dipole–dipole array used in the model study, which indicates that the conclusions related to the results of Model-1 are independent of the type of measurement configurations.

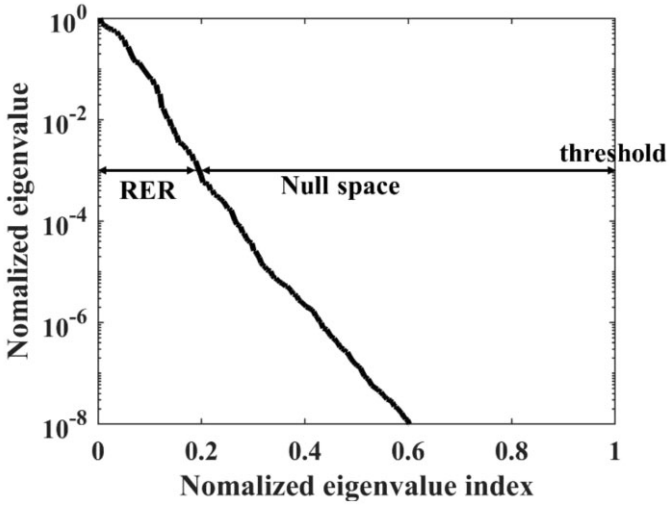

Figure A1. A typical eigenvalue spectrum with the relative eigenvalue range (RER) and the null space indicated.

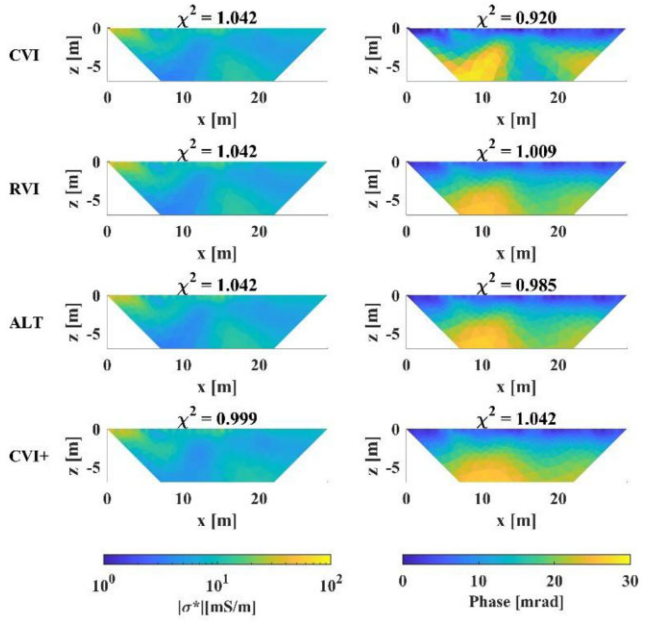

Figure B1. Inversion results obtained by different strategies for the field data set measured in Lozzolo, Italy.

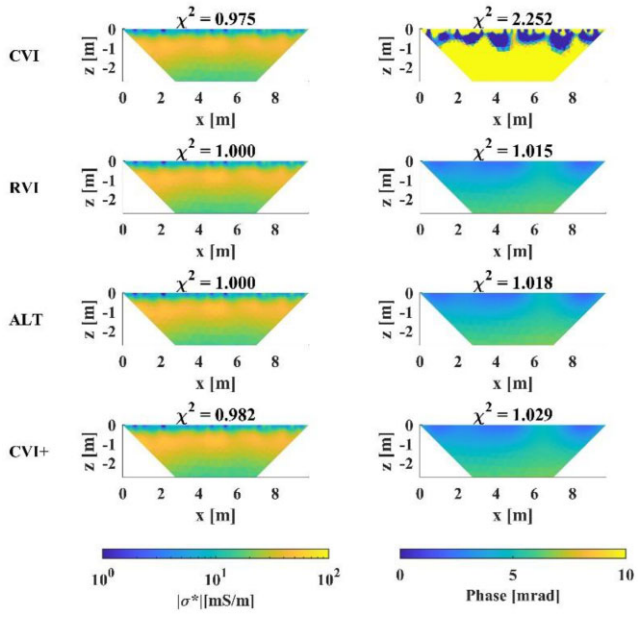

Figure B2. Inversion results obtained by different strategies for the field data set measured in Selhausen, Germany.